

OPTICS

Quantum sensing of strongly coupled light-matter systems using free electrons

Aviv Karnieli^{1†}, Shai Tseses^{2†}, Renwen Yu^{3†}, Nicholas Rivera^{4,5}, Zhexin Zhao³, Ady Arie⁶, Shanhui Fan³, Ido Kaminer^{2*}

Strong coupling in light-matter systems is a central concept in cavity quantum electrodynamics and is essential for many quantum technologies. Especially in the optical range, full control of highly connected multi-qubit systems necessitates quantum coherent probes with nanometric spatial resolution, which are currently inaccessible. Here, we propose the use of free electrons as high-resolution quantum sensors for strongly coupled light-matter systems. Shaping the free-electron wave packet enables the measurement of the quantum state of the entire hybrid systems. We specifically show how quantum interference of the free-electron wave packet gives rise to a quantum-enhanced sensing protocol for the position and dipole orientation of a subnanometer emitter inside a cavity. Our results showcase the great versatility and applicability of quantum interactions between free electrons and strongly coupled cavities, relying on the unique properties of free electrons as strongly interacting flying qubits with miniscule dimensions.

INTRODUCTION

Strong coupling between light and matter systems (1, 2) occurs whenever the rate of their energy exchange exceeds their combined energy loss (3, 4), resulting in hybrid light-matter eigenstates called polaritons (5). This ubiquitous phenomenon has been observed in a wide range of material systems and photon energies (6–10), and in extreme cases, the coupling energies can even reach or exceed the matter and photon energies (11–13). Strong coupling is a deeply ingrained property of cavity quantum electrodynamical (CQED) systems, central to various quantum technologies including quantum computation (14, 15), simulation (16), communication (17), and sensing (18, 19). The latter allows for quantum-enhanced measurement of displacement (20) or frequency (21), as well as accurate reconstruction of the quantum state, if the probe itself is quantum (22).

Current methods for characterizing strongly coupled systems are usually based on optical probes, measuring, e.g., reflection (5), transmission (6), luminescence (23), or scattering (9). That said, the finite spatial extent of a photon (set by the diffraction limit), as well as its transverse polarization, inherently limits information that can be read off of a single emitter (9), such as its position or dipole orientation. Hence, optical probes are typically limited to measuring ensembles of strongly coupled systems. A way to fully characterize strongly coupled systems would have to simultaneously have sufficient spatial resolution while coherently probing the quantum state of the full light-matter system.

In recent years, free electrons have become increasingly appealing in integrated photonic and nanophotonic systems (24, 25),

owing to their subnanometer spatial resolution, allowing detailed probing of subwavelength optical fields. Furthermore, advances in electron energy loss spectroscopy (EELS) reaching few millielectron volt resolution (26) has recently allowed the measurement of the Rabi splitting of cavity polaritons (27, 28). Besides their unmatched spatial resolution, free electrons can also serve as quantum-coherent probes. Ultrafast electron microscopy experiments demonstrated coherent interactions of free electrons and light (29–34) and were also used to probe its quantum photonic nature (35–38).

On the other hand, the idea to use free electrons for coherent interactions with bound electrons was only proposed recently (39). This idea spawned substantial interest and follow-up work (39–44), for example, the proposal to use free electrons for measuring the quantum state of bound-electron systems (40, 42). However, no work so far investigated the coherent and simultaneous quantum interaction of a free electron with strongly coupled systems of light and matter. These interactions can bring insight on inaccessible regimes of CQED (for example, ultrafast imaging of rapid Rabi oscillations), with the vision of deep-subwavelength quantum sensing protocols of strong coupling and the coherent measurement of quantum states of hybrid light-matter systems.

Here, we show how a free electron can be used as a new type of quantum sensor, directly inferring the quantum information embedded in a strongly coupled light-matter system. We demonstrate how a free electron can sense the parameters of the system Hamiltonian, including the complex relative phase of the coupling coefficients. With this capability, we propose a quantum-enhanced sensing protocol for measuring the position and dipole orientation of an emitter inside a cavity. Using shaped free-electron wave packets, we exemplify a scheme to measure the polaritonic quantum state, comprising both the emitter and the field within the cavity. Our results showcase the great versatility and applicability of quantum interactions between free electrons and strongly coupled light-matter systems, relying on the unique properties of the free electron as a strongly interacting flying qubit with miniscule dimensions. We note that the related, complementary paper of Lim *et al.* (43) was released simultaneously with our work.

¹Raymond and Beverly Sackler School of Physics and Astronomy, Tel Aviv University, Ramat Aviv 69978 Tel Aviv, Israel. ²Andrew and Erna Viterbi Department of Electrical and Computer Engineering, Technion–Israel Institute of Technology, Haifa 32000, Israel. ³Department of Electrical Engineering, Stanford University, Stanford, CA 94305, USA. ⁴Department of Physics, Massachusetts Institute of Technology, Cambridge, MA 02139, USA. ⁵Department of Physics, Harvard University, Cambridge, MA 02138, USA. ⁶School of Electrical Engineering, Fleischman Faculty of Engineering, Tel Aviv University, 69978 Tel Aviv, Israel.

*Corresponding author. Email: kaminer@technion.ac.il

†These authors contributed equally to this work.

RESULTS

Theoretical model

We first describe our unified theory for the quantum three-particle interaction of a free electron, a bound electron, and a photon in a single-mode cavity. Assuming that the bound-electron system is a two-level emitter, we can readily use the Jaynes-Cummings (JC) (45, 46) and the free-electron bound-electron resonant interaction (FEBERI) (39–41, 47) models for its coupling to the cavity photon and the free electron, respectively. The coupling of the free electron and the cavity photon is generally captured by the quantum photon-induced near-field electron microscopy (QPINEM) (35, 37, 48, 49) model. This simplified interaction scenario can be extended to include a wide range of models for the emitter-cavity system, including the quantum Rabi model (50, 51) in the case of ultrastrong light-matter coupling (52), the Dicke model (53) in the case of an emitter ensemble, or the Hopfield model (54) for collective matter excitations. The latter model can be used instead of the JC model, for example, in dielectric micro- and nanocavities, thus generating a larger Rabi splitting.

By definition, the optical cavity (mode energy $\hbar\omega$) can be occupied by integer multiples of photons, while the two-level emitter (with an energy level difference equal to $\hbar\omega$) can only be found in the manifold of its two energy eigenstates. In the absence of strong coupling, the free electron can exchange energy quanta with either the cavity mode or the emitter, thus increasing or decreasing its energy by integer multiples of $\hbar\omega$ and giving rise to a typical two-sided infinite energy ladder spectrum (illustrated in Fig. 1A). We denote the dimensionless coupling constants between the free

electron and the emitter as g_{ea} (from here onward, a subscript “a” will stand for a two-level “atom,” although any type of two-level emitter can be considered, and the subscript “e” will denote the free electron) and between the electron and photon as g_{ep} (where the subscript “p” denotes the photon). The coupling between the emitter and the cavity is given by the vacuum Rabi frequency Ω_{ap} , arising from the JC model. The resulting three-particle interaction and its three interaction parameters are summarized in Fig. 1.

Figure 1A presents an illustration of the strongly coupled light-matter system of a single emitter and a single-mode cavity probed by a quantum free electron. The example in Fig. 1A is of a molecular emitter placed between a plasmonic nanoparticle and a mirror (9). Our model can be implemented using various other optical cavities, such as dielectric microcavities (10, 55, 56), photonic crystal cavities (57–59), or other plasmonic nanocavities (9, 60–65). Our results below will be focused on deep-subwavelength cavities (9, 57–64) having a large Rabi splitting on the order of 0.1 eV (9, 62–64) [these values were recently observed using EELS (28)] and whose large field confinement can readily compensate the typical free-electron–photon momentum mismatch. We first consider an ideal, lossless cavity for the sake of simplicity. In the last section of this paper, we show that the incorporation of cavity losses needs not alter the main conclusions of our work.

The JC model results in an anharmonic energy ladder of the strongly coupled system within the cavity, wherein each bare cavity energy level is split into two hybrid, light-matter branches: upper and lower polaritons (see inset Fig. 1A). The system has a ground state $|g,0\rangle$ and excited states $|n\pm\rangle = (|g,n\rangle \pm |e,n-1\rangle)/\sqrt{2}$ of

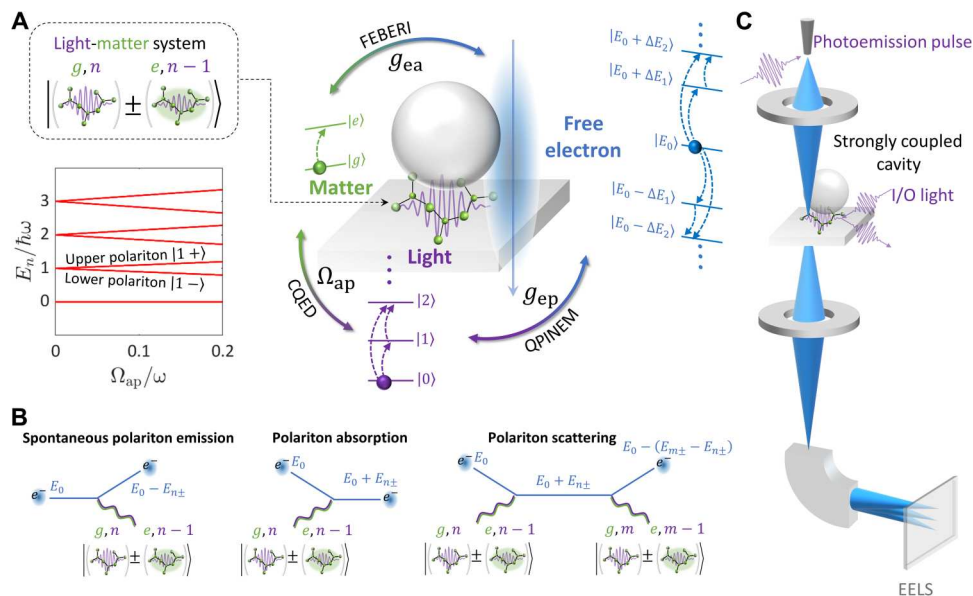


Fig. 1. Coherent free-electron interactions with strongly coupled cavity systems. (A) A free-electron wave function passes by a cavity hosting a single-mode light field and a single emitter [here, without loss of generality, illustrating a molecule in a nanoparticle-on-gold configuration (9)]. The couplings between the electron and light, electron and matter, and matter and light, are g_{ep} , g_{ea} , and Ω_{ap} , respectively. These coupling constants characterize three distinct physical phenomena that are typically considered in isolation: QPINEM is characterized by g_{ep} ; FEBERI is characterized by g_{ea} ; CQED is characterized by Ω_{ap} . Here, these effects occur simultaneously and are coupled to each other. Insets show the cavity polariton states and the energy spectrum in the JC model used to describe the interaction of a two-level system with a single-mode cavity. (B) Effective Feynman diagrams illustrating the free-electron (blue solid lines) interaction with the cavity polaritons (violet and green wavy lines): Spontaneous emission, absorption, and scattering of polaritons are depicted. Note the anharmonic energy changes experienced by the free electron. (C) Proposed experimental setup in ultrafast transmission electron microscopy (UTEM), with input/output (I/O) quantum light impinging at, or extracted from, the sample where quantum interference will be manifested in the measured electron energy loss spectrum (EELS).

frequencies $\omega_{n\pm} = n\omega \pm \sqrt{n}\Omega_{\text{ap}}$, where $n = 1, 2, \dots$ is the number of photons in the cavity. The separation between polariton energies (the Rabi splitting) as a function of the Rabi frequency is depicted in the inset of Fig. 1A. When interacting with the cavity, the free electron spontaneously emits and absorbs polaritons and performs stimulated emission of polaritons and scattering (most dominantly of the same branch), as depicted by the Feynman diagrams in Fig. 1B. In contrast with the conventional case of free-electron interaction with a bare cavity (35), here, the resulting free-electron energy ladder displays uneven spacings, owing to the many possible energy transitions between different polaritonic states.

In what follows, we use a split-step numerical simulation solving for the dynamics of our three-particle system under the interaction Hamiltonian. The three parts of the system are the free electron [energy ladder operators b_q, b_q^\dagger for electron recoil $\hbar q$ (35)], the emitter (raising and lowering operators σ_+, σ_-), and the cavity photon (annihilation and creation operators a, a^\dagger). These are coupled by the interaction Hamiltonians $H_{\text{ep}} = iv \int dq g_{\text{ep}}(q) ab_q^\dagger + h.c.$ (electron-photon coupling), $H_{\text{ea}} = iv \int dq g_{\text{ea}}(q) \sigma_- b_q^\dagger + h.c.$ (electron-emitter coupling), and $H_{\text{ap}} = \Omega_{\text{ap}} \sigma_+ a + h.c.$ (emitter-photon coupling). The three

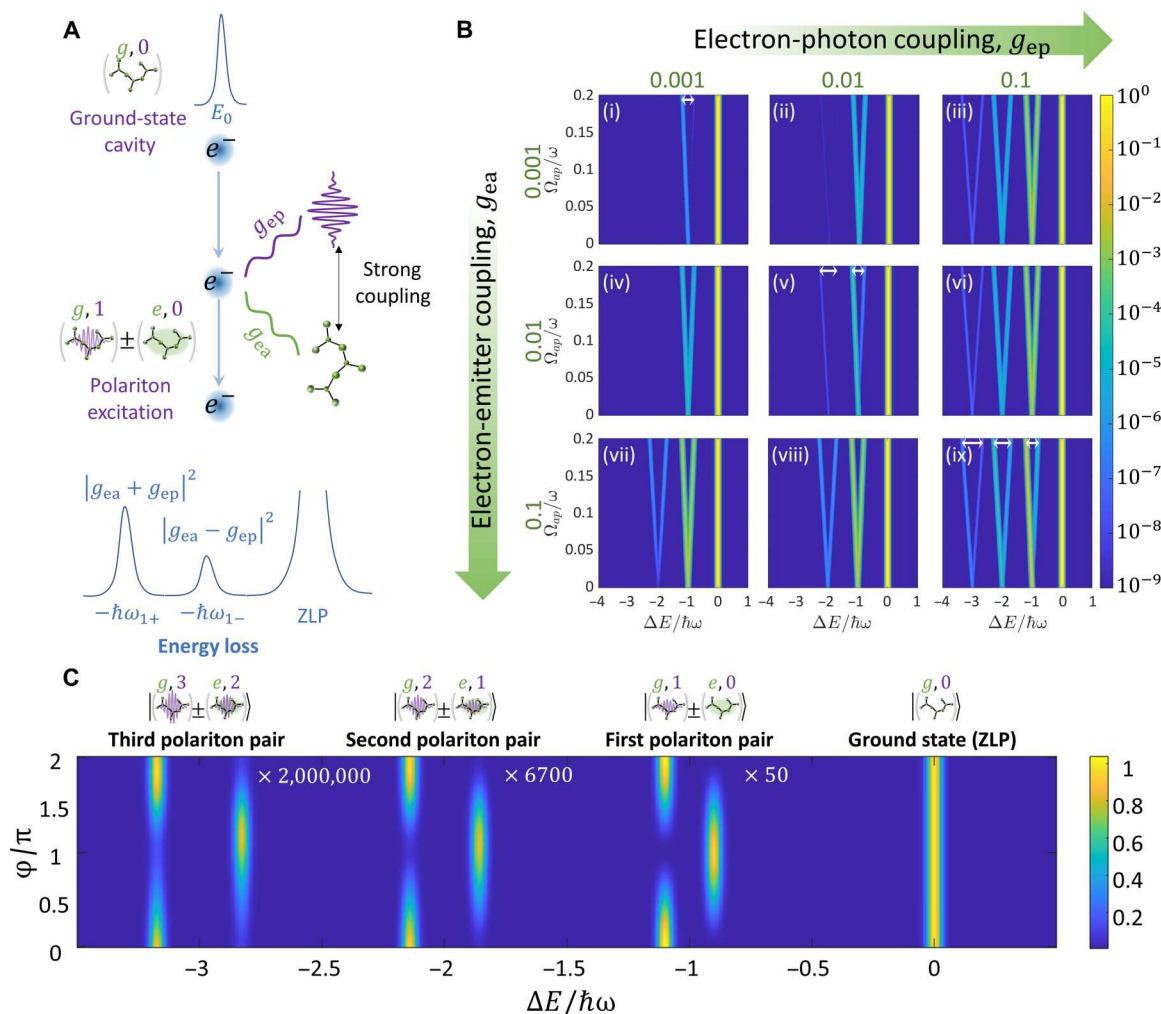


Fig. 2. Electron energy loss and quantum interference following spontaneous polariton emission. (A) Schematic depiction of the coherent interaction between a free electron and a strongly coupled cavity, with the electron coupled simultaneously to the light and the emitter. The polariton emission probability then demonstrates interference between the two interaction mechanisms. (B) Simulated EELS (log scale) presented for multiple combinations of the three coupling constants, where g_{ep} and g_{ea} are both real valued and positive. The structure of the anharmonic JC energy ladder (Fig. 1A) is recovered, showing distinct polaritonic branches. Note the asymmetry (marked in white arrows) between polariton branches when g_{ep} and g_{ea} have similar magnitudes: As depicted in (A), this effect originates from quantum interference between the two emission channels. (C) Simulation of spontaneous polariton emission peaks as a function of the relative phase ϕ between g_{ep} and g_{ea} for the case $|g_{\text{ep}}| = |g_{\text{ea}}| = 0.1$ and $\Omega_{\text{ap}} = 0.1\omega$ (see Eq. 1). The first-order polariton emission agrees with the perturbative analytic solution (Eq. 2). Our full simulations unveil similar oscillation also in the higher-order polariton emission. Cavity length of 50 nm, photon wavelength of 532 nm, zero emitter-cavity detuning, initial electron energy $E_0 = 200$ keV, and energy uncertainty of the zero-loss peak (ZLP) of 50 meV.

complex coupling constants g_{ep} , g_{ea} , and Ω_{ap} are given by

$$g_{ep}(q) = \frac{e}{\hbar \omega} \int dze^{-iqz} \mathcal{E}_z(\mathbf{r}_e, z) \quad (1A)$$

$$g_{ea}(q) = \frac{1}{\hbar v} \int dze^{-iqz} V_{ea}(\mathbf{r}_e - \mathbf{r}_a, z) \quad (1B)$$

$$\Omega_{ap} = -\frac{1}{\hbar} \mathbf{d} \cdot \mathcal{E}(\mathbf{r}_a) \quad (1C)$$

In the above definitions, e , v , and z are the electron charge, velocity, and propagation coordinate, respectively; $\mathcal{E}(\mathbf{r})$ is the cavity mode envelope $\mathcal{E}(\mathbf{r}) = \sqrt{\omega/2\epsilon_0} \mathbf{u}(\mathbf{r})$, where $\mathbf{u}(\mathbf{r})$ is a normalized mode function; \mathbf{r}_e and \mathbf{r}_a are the free electron and emitter transverse positions (transverse to z) inside the cavity; \mathbf{d} is the transition dipole moment of the emitter; and V_{ea} is an electrostatic interaction potential between the free electron and the emitter (39–41). The above interaction Hamiltonians and couplings are given in their momentum-space form; for the position-space representation, see the “Real-space interaction Hamiltonians” section in Materials and Methods. Sections S1 to S3 contain the full derivation of the dynamics of the three-particle system.

From here onward, and without loss of generality, we shall assume the Rabi frequency Ω_{ap} to be a positive real number. Of particular importance are the complex electron-photon and electron-emitter coupling strengths, g_{ep} and g_{ea} , which describe the two mechanisms that contribute to free-electron–polariton interaction. In this work, unless explicitly stated otherwise, we consider typical values of electron-photon couplings g_{ep} of the order of 10^{-3} and maximal electron-emitter couplings g_{ea} of the order of 10^{-4} to 10^{-3} (see the “Typical coupling values” section in Materials and Methods for details). Below, we harness the quantum interference between these two coupling constants and their dependence on electron and emitter positions within the cavity, which enable quantum sensing schemes using the free-electron probe.

Sensing complex coupling strengths through quantum interference

Resolving the magnitudes and relative phases of the coupling constants for the two mechanisms that contribute to electron-polariton interaction is what ultimately enables quantum sensing with free electrons, and it is therefore our first objective. The basics of this effect are portrayed in Fig. 2A. A free-electron wave packet interacts with a strongly coupled light-matter system. The free electron can coherently interact with the cavity polaritons through its coupling with both the photon and the emitter. These two couplings can create transitions of the initial electron-polariton states into the same final state. When this happens, the two transition amplitudes (coming from these two coupling mechanisms) can interfere.

More generally, these types of interference effects—on which we base our proposed quantum sensing protocols—can also include a synchronized excitation of the system by external light before the free-electron probe. This can be realized, for example, in ultrafast transmission electron microscopy (UTEM), as depicted in Fig. 1C. In such experiments, a free electron is synchronously photoemitted by a laser pulse and then focused at the sample plane containing the strongly coupled cavity. Quantum light can either be

coupled into or out of the cavity, to excite or to be extracted from the system, respectively. Following the interaction, the free electron is subject to the EELS measurement, where the interference effect is manifested.

To theoretically demonstrate this interference effect, we turn to our fully quantum simulation. In Fig. 2B, we plot the simulated EELS spectra following spontaneous polariton emission for different coupling regimes, showcasing how a free electron can coherently couple to several polaritonic branches simultaneously. In general, we observe that when the Rabi frequency Ω_{ap} is increased, the EELS peaks split by $2\hbar\Omega_{ap}$ (see Fig. 2B), with the peaks corresponding to the generation of upper and lower polaritons, respectively. When one coupling dominates, i.e., $|g_{ep}| \gg |g_{ea}|$ (Fig. 2B, ii, iii, and vi) or $|g_{ep}| \ll |g_{ea}|$ (Fig. 2B, iv, vii, and viii), the amplitude of each peak is approximately proportional to the square modulus of the dominant coupling constants. In this regime, the free electron excites the upper and lower polaritons with comparable efficiency, and thus, both polariton peaks are approximately equal in amplitude.

However, we can consider the case when the two couplings g_{ep} and g_{ea} are comparable in magnitude, which may be possible to obtain when the free-electron–light coupling is weak [of the order of 10^{-3} to 10^{-4} ; see (66)] and when the transition dipole moment exceeds tens of debye. In this case, an asymmetry appears between the excitations of the upper and lower polaritons (see Fig. 2B, i, v, and ix). Because the upper and lower polariton eigenstates are entangled superpositions of bare photonic and emitter states (with phase differences of 0 and π , respectively), the emission of upper polaritons is favored when g_{ep} and g_{ea} are in phase ($g_{ep} = g_{ea}$), as depicted in Fig. 2A. The relative phase between the two coupling constants is important as it determines the quantum interference of the final free-electron energy states. The phase can be adjusted in several ways: by changing the emitter dipole orientation, by changing the relative position between the free-electron probe and the emitter, and by changing the free-electron probe position inside the cavity field. Another way of actively adjusting quantum interference is to consider a preshaped electron, as discussed in an ensuing section and in section S6.

To further investigate this effect, without loss of generality, we set $g_{ep} = |g|$ and $g_{ea} = |g|e^{i\phi}$ and simulate the EELS as a function of the relative phase ϕ . The results are depicted in Fig. 2C that shows interference in the EELS peaks corresponding to spontaneous emission of upper and lower polaritons, evident in all the polariton branches. This conclusion can also be arrived at analytically by means of first-order perturbation theory (see section S5) with an initial quasi-monochromatic electron of wave function $\psi_{el}(E) = \int dt e^{iEt/\hbar} \psi(z - vt)$ (in the energy domain), yielding a loss probability of

$$p_{\text{loss}}(E) = 2|g|^2 |\psi_{el}(E + \hbar\omega_+)|^2 \cos^2 \frac{\phi}{2} + 2|g|^2 |\psi_{el}(E + \hbar\omega_-)|^2 \sin^2 \frac{\phi}{2} \quad (2)$$

Equation 2 shows a good agreement with the simulation results for the emission of the first polariton pair. The numerical simulation reveals a further phase offset and loss of visibility in the quantum interference at higher-order processes (seen in the second and third polariton pair emission, although they are

considerably less efficient than the first-order process), owing to their nonlinear dependence on the complex coupling coefficients.

Quantum-enhanced sensing protocol of emitter position and dipole orientation inside a strongly coupled cavity

Equipped with the capability to coherently sense the electron-polariton coupling, we now propose a way to exploit the resulting quantum interference to characterize strongly coupled systems with superior spatial resolution. Determining the position of subnanometer emitters inside a cavity using an optical probe is a challenging task because of the diffraction limit. When using a free-electron probe for this task, it is crucial to analyze the signal-to-noise ratio (SNR) to find the detection limits. The SNR is limited by the (usually low) inelastic scattering cross section between the electron and the emitter (40, 41), by thermal noise (dark counts) in the electron detector (67, 68) and by Poissonian shot noise in the electron detector signal originating from more dominant inelastic scattering processes. To overcome the challenges coming from these noise sources, we propose to use quantum interference effects within EELS to allow quantum-enhanced sensing (18, 69) of the emitter position and even its dipole orientation. Specifically, we show in this section how energy-filtered imaging (70–73) enables to extract this information with the spatial resolution of electron microscopes.

Our sensing protocol relies on the quantum interference of the electron wave function with itself and on the spatial dependence of g_{ep} , g_{ea} , and Ω_{ap} . The same quantum enhancement (QE) factor appears in two ways: (i) enhancement of the absolute signal level, as compared to imaging a bare emitter in the absence of strong coupling (important for surpassing detector thermal noise) and (ii) enhancement of SNR in the presence of shot noise, as compared to a measurement that does not exploit quantum interference. Examples for such measurements are the loss signal from either polariton branch alone $P_{1\pm}$ and the total polariton loss signal $P_{tot} = P_{1+} + P_{1-}$. When the electron-photon coupling is much stronger than the electron-emitter coupling, these observables will not exhibit interference, and the emitter signal will be obscured by the shot noise. Below, we will compare the SNR of the total polariton loss signal P_{tot} with the difference between polariton loss signals, $P_{diff} = |P_{1+} - P_{1-}|$, and show the advantage gained from quantum interference, which plays a role only for P_{diff} .

Figure 3 (A and B) illustrates the proposed experimental scenario. We consider a nanoscale emitter coupled to an optical cavity and located at \mathbf{r}_a . A free-electron beam at a varying lateral position \mathbf{r}_e scans over the whole system, as can be done routinely in scanning transmission electron microscopes. We are interested in showing how the resulting spatially dependent EELS can demonstrate enhanced sensing for different emitter locations. We first reiterate that the total electron energy loss probability P_{tot} , which integrates over the two polariton EELS peaks, shows no interference effects (as discussed in section S6.C). Rather, the sensing protocol we describe relies on the difference $P_{diff} = |P_{1+} - P_{1-}|$ between the upper and lower polaritonic electron loss probabilities. In Fig. 3, we assume that the scan is performed using an ensemble of N identical monoenergetic electrons with an initial wave function $\psi_{el}(E)$ and introduce Poissonian noise in the calculated energy-filtered images, as is usually the case for electron spectrometer cameras (74). Each electron interacts independently with a ground-state cavity $|g, 0\rangle$, i.e., the time between consecutive electrons is much larger than the cavity

polariton lifetime. After the interaction, we measure EELS and observe the first two polariton peaks (similarly to Fig. 2B). The differential signal P_{diff} is analytically calculated using first-order perturbation theory (see detailed derivation in section S6) and is proportional to an interference term between the two emission mechanisms, namely

$$P_{diff}(\mathbf{r}_e|\mathbf{r}_a) = 2|\text{Re}[g_{ep}(\mathbf{r}_e)g_{ea}^*(\mathbf{r}_e - \mathbf{r}_a)]|\text{erf}\left(\frac{\hbar\Omega_{ap}(\mathbf{r}_a)}{\sqrt{2}\Delta\epsilon}\right) \quad (3)$$

In the above equation, we assume that $\psi_{el}(E)$ is Gaussian, $\Delta\epsilon$ is the electron energy uncertainty, and erf denotes the error function (as discussed in the final section of this paper, incorporation of cavity losses may broaden the EELS peaks beyond $\Delta\epsilon$, depending on the cavity lifetime). In the more common case where the electron-photon coupling is larger than the electron-atom coupling (here, we again consider g_{ep} of the order of 10^{-3} and a maximal value of g_{ea} of 10^{-4}), the signal in Eq. 3 resembles a homodyne amplification wherein the strong electron-photon interaction g_{ep} takes the role of a local oscillator, g_{ea} acts as the amplified signal, and the free electron acts as the beam splitter.

The QE factor of the difference signal P_{diff} of Eq. 3, over the total signal P_{tot} , is given by

$$\text{QE} = \frac{|g_{ep}|}{|g_{ea}|} |\cos[\arg(g_{ep}g_{ea}^*)]| \text{erf}\left(\frac{\hbar\Omega_{ap}}{\sqrt{2}\Delta\epsilon}\right) \quad (4)$$

The above equation has implicit dependence on the electron and emitter positions through the coupling coefficients. Maximal QE is achieved at $\mathbf{r}_a = \mathbf{r}_e$ and when g_{ep} and g_{ea} are in phase (we note that the latter requirement can be relaxed by using a generalized sensing protocol using shaped free electrons and an excited emitter, reaching the maximal value of QE for any value of $\arg(g_{ep}g_{ea}^*)$. For details, see the subsequent section, section S6.D, and eq. S116.16). Figure 3C plots Eq. 4 against the ratios $|g_{ep}/g_{ea}|$ and $\hbar\Omega_{ap}/\Delta\epsilon$ for an ideal case of $\arg(g_{ep}g_{ea}^*) = 0$ or π . The white dashed line marks the transition to $\text{QE} > 1$, requiring that the electron-photon coupling will be stronger than the electron-emitter coupling ($|g_{ep}| > |g_{ea}|$), and that the two polariton peaks could be resolved by EELS, namely, that $\hbar\Omega_{ap} > \Delta\epsilon$. When losses are present, the latter condition should be amended such that the Rabi splitting is larger than the total broadening caused by both the electron energy uncertainty and polariton linewidths (as discussed in the final section and in section S7).

To illustrate the quantum-enhanced signals, Fig. 3 (D and E) depicts two-dimensional (2D) scan images of the total (Fig. 3D) and differential (Fig. 3E) signals, as calculated analytically, and in the presence of shot noise. A ratio of $|g_{ep}|/|g_{ea}| \sim 10$ was assumed, as well as an out-of-plane emitter dipole moment (i.e., pointing along the electron propagation direction), with $\arg(g_{ep}g_{ea}^*) = 0$ and $N = 10^9$ electrons. If one were to use the total signal P_{tot} for imaging, then the emitter signal $N|g_{ea}|^2$ would have been completely obscured by the background shot noise $\sqrt{N}|g_{ep}|$ (Fig. 3D, i). For a bare emitter (Fig. 3D, ii), the total signal level is more than an order of magnitude weaker compared to the quantum-enhanced difference signal. The difference signal (Fig. 3E), on the other hand, enjoys an enhancement factor given by Eq. 4 (see section S6 for derivation), allowing an increase by $|g_{ep}|/|g_{ea}| \sim 10$ in SNR [Fig. 3E (i) compared to Fig. 3D (i)] and in absolute signal level (compared

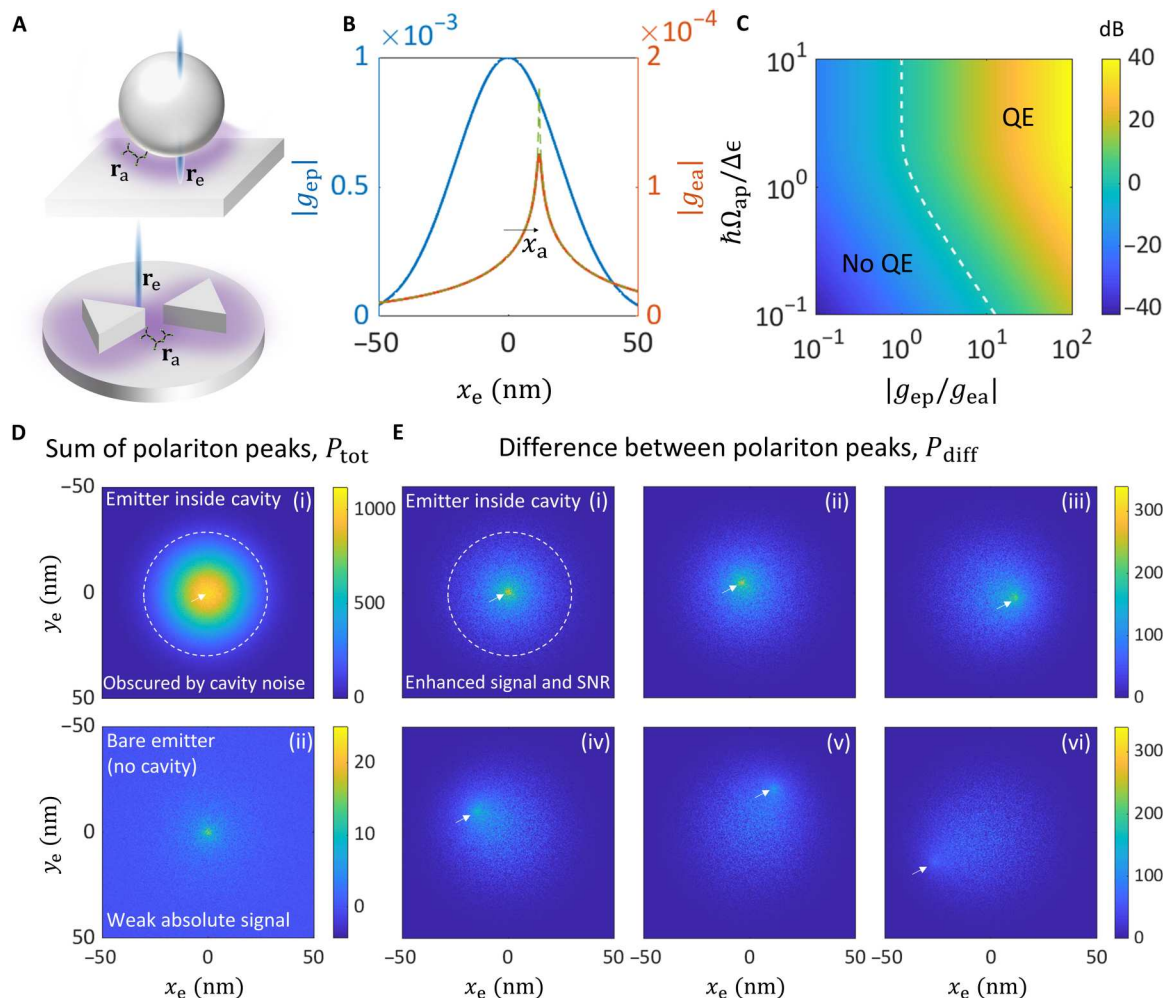


Fig. 3. Free-electron quantum-enhanced sensing of emitter position inside a strongly coupled cavity. (A) Schematic depiction of our quantum sensing protocol (\mathbf{r}_e , free-electron probe position; \mathbf{r}_e , emitter position). (B) Spatially dependent coupling strengths (explicit expression for g_{ea} given in section S4) as a function of the electron position x_e and for a specific emitter displacement (here, the emitter is located 12 nm from the cavity center, and its transition dipole was oriented along the z direction). (C) QE as a function of the coupling ratio $|g_{ep}/g_{ea}|$ and the strong coupling normalized by electron energy uncertainty $\hbar\Omega_{ap}/\Delta\epsilon$, according to Eq. 4. White dashed line marks the transition to QE > 1 . (D and E) Analytically calculated 2D scan images in the presence of shot noise, assuming $N = 10^9$ electrons with maximal ratios of $|g_{ep}/g_{ea}| = 10$ and $\hbar\Omega_{ap}/\Delta\epsilon = 4.7$ (at $\mathbf{r}_e = \mathbf{r}_a = 0$). White dashed circles mark the cavity mode transverse envelope, and white arrows mark the point-like emitter position. (D) Total signal P_{tot} for two different cases: (i) an emitter situated at a cavity center and (ii) a bare emitter (no cavity). In (i), the emitter signal is obscured by the background noise, and in (ii), the absolute signal level is an order of magnitude weaker than the quantum-enhanced signal. (E) Difference signal P_{diff} for different emitter positions with increasing distance from the cavity center. Comparing (E, i) with (D, i) and (D, ii), both the SNR and the absolute signal level are enhanced by a factor of $|g_{ep}/g_{ea}| = 10$. SNR degrades as the emitter moves away from the center (ii) to (vi).

to Fig. 3D, ii). Figure 3E(ii to vi) depicts the enhanced signal for different emitter positions. The emitter is easier to detect when it and the electron probe are placed near the center of the cavity $\mathbf{r}_e = \mathbf{r}_a = 0$, where both $|g_{ep}|$ and Ω_{ap} are maximal. The contrast reduces for emitters positioned away from the center. In the absence of strong coupling (i.e., $\Omega_{ap} \approx 0$), the difference signal P_{diff} of Eq. 3 vanishes, whereas the total signal P_{tot} remains the same. This fact indicates that strong coupling plays an essential role in our quantum sensing scheme: Only in its presence can we resolve the desired quantum interference.

The emitter position is not the only observable, whose detection can be enhanced by the quantum interference: The proposed differential measurement is also sensitive to the emitter dipole orientation (direction of its transition dipole moment), as explored in

details below. This effect relies on the fact that the phase of the complex electron-emitter coupling g_{ea} depends on the emitter's dipole orientation (see section S4) and that the enhancement (Eq. 4) is sensitive to this phase dependence through the $\cos[\arg(g_{ep}g_{ea}^*)]$ term.

To show the quantum-enhanced detection of the emitter dipole moment orientation, we performed numerical simulations of line-scan imaging according to the above sensing protocol. We first assume an in-plane emitter dipole moment. For an in-plane dipole, the free-electron-emitter coupling g_{ea} is real valued, and its spatial dependence resembles the derivative of a Lorentzian function (see section SI4) that vanishes at the emitter position. For the homodyne-like QE, we require that $\arg(g_{ep}g_{ea}^*) = 0$ or π (see Eq. 3), and thus for an enhanced in-plane dipole signal, g_{ep} must also be

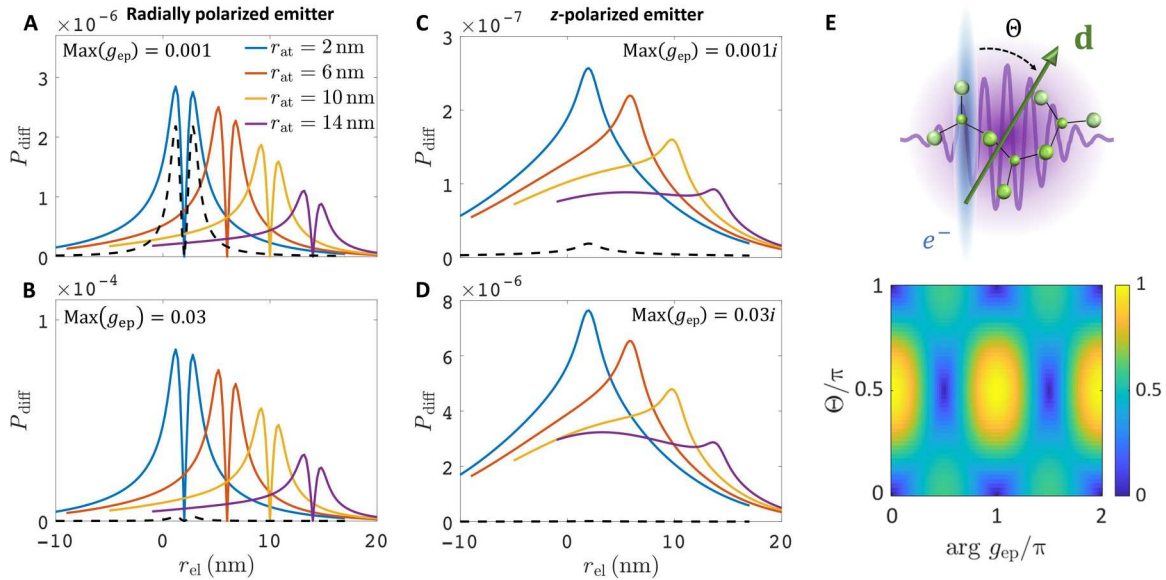


Fig. 4. Quantum sensing of emitter dipole orientation by free electrons. (A to D) Numerical simulations of the free-electron energy loss probability difference P_{diff} as a function of electron beam position \mathbf{r}_e , scanned along the radial direction of the optical cavity (see schematics in Fig. 3A) for four different emitter locations \mathbf{r}_a : 2 nm (blue curve), 6 nm (red curve), 10 nm (orange curve), and 14 nm (purple curve). The black dashed curve represents a reference loss probability of a bare emitter (no cavity) located at $\mathbf{r}_a = 2$ nm. In (A), the dipole moment of the emitter is assumed to be along the radial direction (in plane). Here, we also assume a transversely Gaussian cavity mode profile, resulting in the spatial dependencies of the coupling constants as $g_{\text{ep}}(\mathbf{r}_e) = \eta \exp(-r_e^2/2\sigma^2)$ and $\Omega_{\text{ap}}(\mathbf{r}_a) = 0.1 \exp(-r_a^2/2\sigma^2)$, with $\sigma = 10$ nm and $\eta = 0.001$. Panel (B) is the same as (A) but with $\eta = 0.03$, resulting in a 30-fold increase in QE. Panels (C) and (D) are the same as (A) and (B) but for an emitter dipole moment along the z direction (out of plane). In (C) and (D), we assume $\eta = 0.001i$ and $0.03i$, respectively, where an imaginary value for g_{ep} is needed in this case to enable quantum-enhanced sensing. Cavity length of 10 nm, photon wavelength of 532 nm, zero emitter-cavity detuning, initial electron energy $E_0 = 200$ keV, and energy uncertainty of 50 meV. (E) Analytically calculated quantum-enhanced signal P_{diff} (averaged over electron position and normalized) as a function of emitter dipole orientation angle, Θ (top inset), and the phase of the electron-photon coupling g_{ep} for $|g_{\text{ep}}| = 0.001$ and $|\mathbf{d}| = 3.8$ debye.

real. As mentioned above, this requirement on $\arg(g_{\text{ep}}g_{\text{ea}}^*)$ can be relaxed by generalizing the sensing protocol (as detailed in the next section and in section S6.D). In Fig. 4A, we plot the absolute value of $P_{\text{diff}}(\mathbf{r}_{\text{el}}|\mathbf{r}_a)$ (solid curves), scanning the free-electron probe position \mathbf{r}_e along the radial direction of the optical cavity for different emitter locations \mathbf{r}_a along the same radius. The enhancement with respect to a bare emitter signal (black dashed curves) increases markedly when the maximal value of g_{ep} is increased, as shown in Fig. 4B.

When the emitter dipole moment is out of plane, g_{ea} is generally weaker and becomes purely imaginary with a spatial dependence that resembles a Lorentzian function (see section S4). If g_{ep} is real valued, then this time $\arg(g_{\text{ep}}g_{\text{ea}}^*) = \pi/2$, and thus according to Eq. 3, the differential signal vanishes. In Fig. 4 (C and D), g_{ep} is chosen instead as purely imaginary to ensure quantum-enhanced sensing. Thus, similar to the case of Fig. 4B, Fig. 4 (C and D) presents strong quantum-enhanced signals P_{diff} relative to the bare emitter signal. The smallness of g_{ea} for an out-of-plane dipole allows for a strong homodyne-like amplification already for a much weaker value of g_{ep} . In Fig. 4E, we plot the position-averaged quantum-enhanced signal P_{diff} as a function of emitter dipole orientation angle Θ and as a function of the phase of the electron-photon coupling g_{ep} , demonstrating the direct sensitivity to the emitter dipole orientation angle.

We end this subsection by noting that similar interference features could be predicted by a semiclassical theory, where one replaces the free-electron probe by a continuous charge density and the light-matter system by a classical dipole inside an optical cavity.

The interference is then manifested in the difference signal P_{diff} , as optical interference of the reflected field back-acting on the free electron. However, such a model is inherently limited as it cannot capture important quantum features that we use in other sensing protocols, as in the ensuing section (Fig. 5). These include coherent free-electron wave function shaping (Fig. 5A), quantum state interrogation (Fig. 5, B and C), photon statistics, entanglement between the free-electron probe and the polaritonic system, decoherence of quantum information, and higher-order effects (Fig. 2). For these reasons, we choose here to provide a fully quantum description to all of our quantum sensing protocols.

Sensing of polariton quantum states

The quantum interference effects we used thus far were for a strongly coupled light-matter system initially in its ground state. However, these effects can also be used when the system is excited to a certain hybrid quantum light-matter state. In principle, the excited state can be reconstructed by free-electron measurements through preshaping of the electron wave packet, followed by electron energy measurement. To do this, consider two (or more) possible polaritonic transitions. Interference between the different transition amplitudes is manifested in the electron energy spectrum and allows access to the complex amplitudes of the initial polariton state. Because the polariton is not directly measured, it is necessary to avoid entanglement between the free electron and the polariton following the transitions of interest. Because we measure only the final state of the free-electron wave function, we discard any information regarding the final state of the polaritons, such that

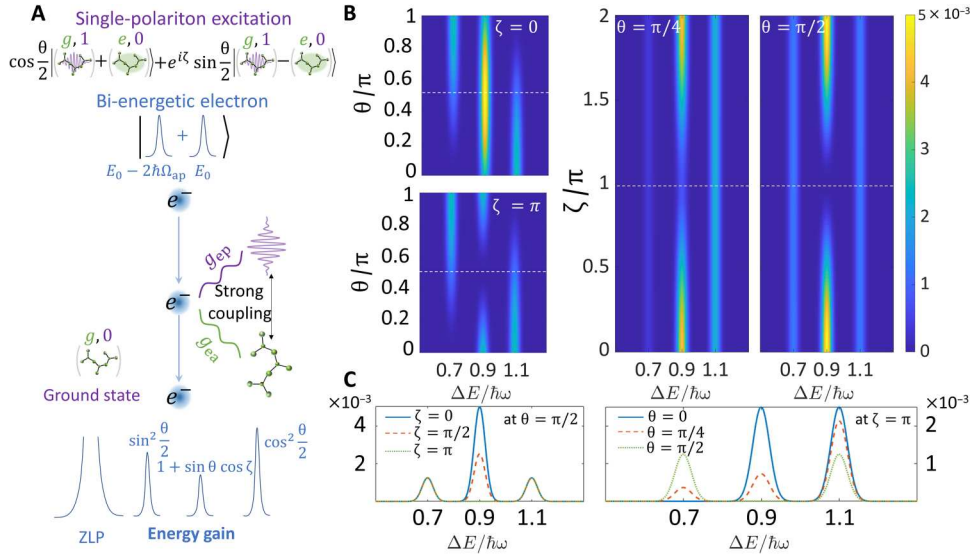


Fig. 5. Sensing the quantum state of cavity polaritons using free electrons. (A) Schematic depiction of the interaction between a bi-energetic free electron (energy separation $2\hbar\Omega_{ap}$) and a strongly coupled cavity hosting a single-polariton superposition state $\cos\theta/2|1+\rangle + e^{i\zeta}\sin\theta/2|1-\rangle$. The energy gain peaks can then reveal the quantum state of the cavity. (B) Simulation of single-polariton absorption peaks, as a function of the angles θ and ζ defining the polariton state. Left (right): Energy gain peaks for two values of fixed ζ (θ) as a function of θ (ζ). The central peak demonstrates interference with respect to both θ and ζ , while the outer peaks correspond to interference with respect to θ . (C) Cross sections of the simulation scans in (B) (marked in white dashed lines) for a fixed value of θ (left) and ζ (right). Cavity length of 50 nm, photon wavelength of 532 nm, zero emitter-cavity detuning, initial electron energy $E_0 = 200$ keV, energy uncertainty of 50 meV, and coupling constants $g_{ep} = 0.1$, $g_{ea} = 0$.

quantum decoherence may limit the amount of information to be extracted about the polaritonic initial state. This can be avoided, however, by considering transitions from different initial states that share the same final polariton state, such as the ground state.

To exemplify this concept, consider the polariton state $|\psi_{cav}\rangle = \cos\frac{\theta}{2}|1+\rangle + e^{i\zeta}\sin\frac{\theta}{2}|1-\rangle$, defined by the angles ζ and θ . This qubit state is of practical interest for quantum information processing using CQED (17), constituting an entangled state of the emitter and photon. Alternatively, one could write this state explicitly as a bipartite entangled state $|\Psi\rangle = c_+|1g\rangle + c_-|0e\rangle$ and ask whether the electron can infer the complex-valued coefficient c_{\pm} . We wish to measure the parameters ζ and θ using a preshaped free electron in a superposition of two energies, $|\psi_{el}\rangle = \frac{1}{\sqrt{2}}|E_0\rangle + \frac{1}{\sqrt{2}}|E_0 - 2\hbar\Omega_{ap}\rangle$ having an envelope $\psi_{el}(E)$. The shaped free electron probes the system (Fig. 5A). We consider the case of polariton absorption (electron energy gain) for which the final state of the cavity is $|g, 0\rangle$ for both transitions. We calculate perturbatively the energy gain probability upon absorption of the single polariton by the electron, yielding (for the typical case of $|g_{ep}| \ll |g_{ea}| = |g|$)

$$\begin{aligned}
 p_{\text{gain}}(E) &= \frac{1}{4}|g|^2 \sin^2 \frac{\theta}{2} |\psi_{el}(E - \hbar\omega + 3\hbar\Omega_{ap})|^2 \\
 &+ \frac{1}{4}|g|^2 (1 + \sin\theta \cos\zeta) |\psi_{el}(E - \hbar\omega + \hbar\Omega_{ap})|^2 \quad (5) \\
 &+ \frac{1}{4}|g|^2 \cos^2 \frac{\theta}{2} |\psi_{el}(E - \hbar\omega - \hbar\Omega_{ap})|^2
 \end{aligned}$$

The values of θ and ζ of the cavity state $|\psi_{cav}\rangle$ can thus be inferred from the gain probabilities. The above example is numerically verified using our simulation, as depicted in Fig. 5B, where we plot the

electron energy gain spectra for the above initial states and with different values of the angles θ and ζ , demonstrating the expected interference. This simple scheme could also be used to reconstruct a single-polariton mixed state ρ_{cav} . In addition, superpositions of higher-order polaritonic states such as $\alpha|n+\rangle + \beta|n-\rangle$ could be reconstructed using a similar interference mechanism, which necessitates n th order polariton absorption and an initial electron energy separation of $2\sqrt{n}\hbar\Omega_{ap}$. To measure correlations between polaritonic states of different occupation numbers, one needs to consider transitions that leave the cavity at an intermediate joint state and adapt the free-electron wave packet shape accordingly.

As a final remark, we note that the sensing protocol based on shaped free electrons can also resolve the temporal dynamics of ultrafast Rabi oscillations, using a temporal delay between the emitter excitation and the electron arrival time in a UTEM setup (as depicted in Fig. 1C). In this case, the phase angle of the excited quantum state scales as $\zeta = 2\Omega_{ap}\tau$, with τ denoting the arrival time delay, where the modulation is seen on the central gain peak at $E = \hbar\omega - \hbar\Omega_{ap}$. Further, and as detailed in section S6.D, by controlling the time delay (or, equivalently, the relative phase in the initial free-electron energy superposition state), one can extract from the three energy gain peaks both real and imaginary parts of the product $g_{ep}g_{ea}^*$, which was used to obtain the quantum-enhanced signal of Eq. 3. In this manner, the condition on $\arg(g_{ep}g_{ea}^*)$ for achieving QE can be lifted altogether.

The effect of cavity losses

In realistic systems, and particularly in strongly coupled nanoplasmic systems, losses due to finite cavity lifetimes can be substantial. We show in the ‘‘Incorporation of polaritonic losses’’ section in Materials and Methods, that losses do not affect the main

conclusions presented in the above sections. For the quantum sensing of emitter position and dipole orientation based on spontaneous polariton emission, Eq. 10 in Materials and Methods shows that the EELS peaks are broadened by the cavity linewidth, while the transition amplitudes are still proportional to the coherent sum and difference of the two complex coupling constants, as in Fig. 2A. To resolve the two polariton loss peaks and obtain QE, one needs to make sure that the Rabi splitting is not only larger than the electron energy uncertainty (as in Eq. 4) but also larger than the combined energy width broadened by the cavity linewidth.

Losses need not compromise the sensing of polaritonic states, too: Eqs. 11-12 show that this quantum sensing protocol, based on polariton absorption, is applicable also in the presence of losses, as long as the peaks can be resolved considering the linewidth broadening discussed above. A preshaped electron wave function can still coherently recover the polariton state, and the additional broadening due to losses causes no fundamental change in our results.

DISCUSSION

We showed how free electrons can be used as a new type of quantum sensor for strongly coupled cavity systems. By means of numerical simulations and analytic calculations, we demonstrated that electron energy spectroscopy can be used to measure quantum interference between polariton emission mechanisms. Moreover, shaped free electrons can coherently sense the polariton quantum state inside an excited cavity. The latter can be beneficial for readout of quantum information encoded in cavity polaritons (17) and its subsequent transmission using free electrons (40–42, 75, 76). Using the same mechanism, shaped free electrons can also resolve the temporal dynamics of ultrafast Rabi oscillations through the phase angle that scales as $\zeta = 2\Omega_{\text{ap}}\tau$, with τ denoting the electron arrival time delay.

Our work proposed a quantum sensing protocol for measuring the spatial displacement and the dipole orientation of nanoscale emitters strongly coupled to a cavity, leading to QE of both the detected signal and its SNR. The enhancement is attributed to two main factors: the strong coupling and entanglement between the emitter and the photon, as well as the free electron's ability to coherently and simultaneously interact with both constituents of the light-matter system.

We expect that quantum sensing of strongly coupled cavities using free electrons could be experimentally observed in modern electron microscopes and particularly in UTEMs (29, 30, 34, 77–79). Progress in scanning electron microscopes can now also use ultrafast microscopy techniques and EELS (80), thus broadening the possible electron energy range for the proposed experiments. State-of-the-art energy filters can be used to prepare electrons with tens of millielectron volt energy spread, with certain EELS systems reaching as low as few millielectron volt resolution (26, 81) [as used to resolve strong coupling in recent experiments (27, 28)]. Furthermore, a PINEM-type interaction (82, 83) followed by energy filtering could be used to prepare the desired shaped electron required for sensing of polariton quantum states.

The parameters assumed throughout the text are now becoming accessible by progress reported in recent experiments pursuing efficient electron interactions with quantum photonic states of light (37, 84) reaching the single-electron–single-photon regime (84). While it was shown experimentally that free electrons can maintain quantum coherence upon interacting with light (29, 30, 84, 85), we

still need polariton lifetimes and decoherence rates slower than the Rabi frequency to ensure that the EELS peaks could be resolved. Further improving the spectral resolution of future electron microscopes can be used to resolve smaller Rabi splitting, as in the case of single emitters embedded in dielectric nano- and microcavities.

As an extension to our work, phase-matched interactions (85) of free electrons with strongly coupled microcavities could lead to single-photon nonlinearities and photon blockade in electron-photon interactions, as we recently reported (86). Going beyond quantum sensing, we envision quantum information processing and quantum communication between free electrons and cavities (87) to become an important application for our theory. In that sense, the additional polaritonic degree of freedom—for example, an external coherent control over the emitter state—can extend the possibilities of the emerging field of free-electron quantum optics, which until recently considered interactions of free electrons and bare cavities. The techniques reported in our manuscript, together with recent studies on the use of free electrons to entangle distant cavities (87) or matter qubits (41), could be used to entangle distant cavity polaritons as well when postselecting on the final electron energy. Postselection using coincidence detection of photons and free electrons could now be made possible, thanks to a recent experimental realization of coincidence measurements following a quantum PINEM interaction (88). Furthermore, it will be interesting to investigate ensemble sensing (18) using multiple entangled qubits, where we envision the cavity being prepared in a polaritonic N00N state to reach the Heisenberg limit. Alternatively, the use of multiple-electron pulses and even entangled multiple-electron states (35, 89) may prove useful for increasing the coupling strengths and realizing entanglement-enhanced sensing.

MATERIALS AND METHODS

Real-space interaction Hamiltonians

The system Hamiltonian in free-space can be written as

$$H = H_0 + H_{\text{prop}} + H_{\text{JC}} + H_{\text{FEBERI}} + H_{\text{QPINEM}} \quad (6)$$

where

$$H_0 = \hbar \omega a^\dagger a + \frac{\hbar \omega}{2} \sigma_z + E_0 \quad (7)$$

is the free Hamiltonian (E_0 denotes the electron carrier energy, about which we Taylor-expand its kinetic energy operator), and

$$H_{\text{prop}} = \int dz \psi^\dagger(z) (-i\hbar v \partial_z) \psi(z) \quad (8A)$$

$$H_{\text{JC}} = -\mathbf{d}^* \cdot \mathcal{E}^*(\mathbf{r}_a) \sigma_- a^\dagger - \mathbf{d} \cdot \mathcal{E}(\mathbf{r}_a) \sigma_+ a \quad (8B)$$

$$H_{\text{FEBERI}} = \int dz \psi^\dagger(z) (V_{\text{ea}}^*(\mathbf{r}_e - \mathbf{r}_a, z) \sigma_- + V_{\text{ea}}(\mathbf{r}_e - \mathbf{r}_a, z) \sigma_+) \psi(z) \quad (8C)$$

$$H_{\text{QPINEM}} = \int dz \psi^\dagger(z) \left[i \frac{eV}{\omega} \mathcal{E}_z(\mathbf{r}_e, z) a - i \frac{eV}{\omega} \mathcal{E}_z^*(\mathbf{r}_e, z) a^\dagger \right] \psi(z) \quad (8D)$$

are, respectively, the free-electron propagation Hamiltonian, the JC Hamiltonian, the FEBERI Hamiltonian, and the QPINEM

Hamiltonian. Here, $\psi(z)$, $\psi^\dagger(z)$ are the real-space annihilation and creation operators for the free electron in second quantization; v is the carrier electron velocity; \mathbf{d} is the (c-number) emitter transition dipole; $\mathcal{E}(\mathbf{r})$ is the (c-number) cavity mode field envelope; \mathbf{r}_e and \mathbf{r}_a are, respectively, the (c-number) transverse positions of the electron and the emitter inside the cavity; z and $-i\hbar\partial_z$ the electron longitudinal position and momentum, respectively; σ_\pm the emitter raising and lowering Pauli operators; a , a^\dagger are the cavity mode ladder operators; and $V_{ea}(\mathbf{r}) = -\mathbf{d} \cdot \nabla V_{\text{Coul}}(\mathbf{r})$ is the effective potential of the FEBERI interaction, with $V_{\text{Coul}}(\mathbf{r}) = e/4\pi\epsilon_0|\mathbf{r}|$ denoting the Coulomb potential (e is the electron charge and ϵ_0 is the vacuum permittivity).

Typical coupling values

Unless stated otherwise, we consider typical values of electron-photon couplings g_{ep} of the order of 10^{-3} based on the theoretical and experimental study of Yang *et al.* (66) calculating electron energy loss probabilities. We also note that in different geometries, electron-photon couplings as high as 1 were experimentally observed (84). We further consider maximal electron-emitter couplings g_{ea} of the order of 10^{-4} to 10^{-3} for a transition dipole strength of 3.8 debye for the molecule used in (9), with the exact value depending on the transition dipole orientation, electron beam focusing, and relative distance (impact parameter) between the electron and the emitter [for explicit expressions, see section S4 and (39–41)]. To test the effects of stronger electron-photon coupling, g_{ep} of 0.1 was used in Figs. 2 and 5.

Incorporation of polaritonic losses

To incorporate losses, we solve our model dynamics perturbatively where the evolution of the density matrix ρ is governed by the Lindblad equation

$$\dot{\rho} = -\frac{i}{\hbar} [H_0, \rho] + \gamma \sum_i L_i \rho L_i^\dagger - \frac{1}{2} \gamma L_i^\dagger L_i \rho - \frac{1}{2} \gamma \rho L_i^\dagger L_i \quad (9)$$

where H_0 is the unperturbed Hamiltonian of the whole system, with Lindblad jump operators $L_+ = |0\rangle\langle 1+|$ and $L_- = |0\rangle\langle 1-|$ for the JC model (90), having a decay rate γ . The perturbation is introduced via the superoperator $\mathcal{V} = -\frac{i}{\hbar} [H_1, (\cdot)]$, where H_1 is the interaction Hamiltonian between the free electron and the polaritons. Unlike previous derivations in the literature involving EELS from slowly decohering qubits (40, 44), here, we may not neglect the Lindbladian during the interaction time. By moving to Liouville space and formulating a Dyson series in terms of the superoperators, we calculate the spontaneous emission probabilities and the absorption probabilities as in the previous sections. The full derivation appears in section S7. For the spontaneous polariton emission case, we find that

$$p(E) = \int d\epsilon |\Psi_{el}(E + \epsilon)|^2 \left[\frac{1}{2} |g_{ep} + g_{ea}|^2 \frac{1}{\pi} \frac{\hbar\gamma/2}{(\hbar\omega + \hbar\Omega - \epsilon)^2 + (\hbar\gamma/2)^2} + \frac{1}{2} |g_{ep} - g_{ea}|^2 \frac{1}{\pi} \frac{\hbar\gamma/2}{(\hbar\omega - \hbar\Omega - \epsilon)^2 + (\hbar\gamma/2)^2} \right] \quad (10)$$

For the polariton absorption case, exciting a polariton at $t = t_0$ to the state $|\Psi\rangle_{\text{pol}} = \cos\frac{\theta}{2}|1+\rangle + e^{i\kappa}\sin\frac{\theta}{2}|1-\rangle$, we have (again for $|g_{ea}|$

$\ll |g_{ep}| \equiv |g|$)

$$p(E) = \frac{|g|^2}{2} \left| \cos\frac{\theta}{2} c_+(E) + \sin\frac{\theta}{2} e^{i\kappa} c_-(E) \right|^2 \quad (11)$$

where

$$c_\pm(E) = \int \frac{d\epsilon}{2\pi\hbar} \frac{\Psi_{el}(E - \epsilon) e^{i\epsilon t_0/\hbar}}{(\omega \pm \Omega) - \epsilon - i\hbar\frac{\gamma}{2}} \quad (12)$$

Note added in proof: The authors would like to acknowledge the contributions of the following works to this field: Varketina *et al.* (10.1126/sciadv.abq4947), Meier *et al.* (<https://arxiv.org/abs/2209.11806>), and Haindl *et al.* (<https://arxiv.org/abs/2209.12300>).

Supplementary Materials

This PDF file includes:

Sections S1 to S7

REFERENCES AND NOTES

1. Y. Kaluzny, P. Goy, M. Gross, J. M. Raimond, S. Haroche, Observation of self-induced Rabi oscillations in two-level atoms excited inside a resonant cavity: The ringing regime of superradiance. *Phys. Rev. Lett.* **51**, 1175–1178 (1983).
2. G. Rempe, H. Walther, N. Klein, Observation of quantum collapse and revival in a one-atom maser. *Phys. Rev. Lett.* **58**, 353–356 (1987).
3. R. J. Thompson, G. Rempe, H. J. Kimble, Observation of normal-mode splitting for an atom in an optical cavity. *Phys. Rev. Lett.* **68**, 1132–1135 (1992).
4. D. Meschede, H. Walther, G. Müller, One-atom maser. *Phys. Rev. Lett.* **54**, 551–554 (1985).
5. C. Weisbuch, M. Nishioka, A. Ishikawa, Y. Arakawa, Observation of the coupled exciton-photon mode splitting in a semiconductor quantum microcavity. *Phys. Rev. Lett.* **69**, 3314–3317 (1992).
6. A. Wallraff, D. I. Schuster, A. Blais, L. Frunzio, R. S. Huang, J. Majer, S. Kumar, S. M. Girvin, R. J. Schoelkopf, Strong coupling of a single photon to a superconducting qubit using circuit quantum electrodynamics. *Nature* **431**, 162–167 (2004).
7. S. Christopoulos, G. B. H. Von Högersthal, A. J. D. Grundy, P. G. Lagoudakis, A. V. Kavokin, J. J. Baumberg, G. Christmann, R. Butté, E. Feltin, J. F. Carlin, N. Grandjean, Room-temperature polariton lasing in semiconductor microcavities. *Phys. Rev. Lett.* **98**, 126405 (2007).
8. S. Dufferwiel, S. Schwarz, F. Withers, A. A. P. Trichet, F. Li, M. Sich, O. Del Pozo-Zamudio, C. Clark, A. Nalitov, D. D. Solnyshkov, G. Malpuech, K. S. Novoselov, J. M. Smith, M. S. Skolnick, D. N. Krizhanovskii, A. I. Tartakovskii, Exciton-polaritons in van der Waals heterostructures embedded in tunable microcavities. *Nat. Commun.* **6**, 8579 (2015).
9. R. Chikkaraddy, B. De Nijs, F. Benz, S. J. Barrow, O. A. Scherman, E. Rosta, A. Demetriadou, P. Fox, O. Hess, J. J. Baumberg, Single-molecule strong coupling at room temperature in plasmonic nanocavities. *Nature* **535**, 127–130 (2016).
10. J. P. Reithmaier, G. Sęk, A. Löffler, C. Hofmann, S. Kuhn, S. Reitzenstein, L. V. Keldysh, V. D. Kulakovskii, T. L. Reinecke, A. Forchel, Strong coupling in a single quantum dot- semiconductor microcavity system. *Nature* **432**, 197–200 (2004).
11. A. A. Anappara, S. De Liberato, A. Tredicucci, C. Ciuti, G. Biasiol, L. Sorba, F. Beltram, Signatures of the ultrastrong light-matter coupling regime. *Phys. Rev. B* **79**, 201303 (2009).
12. T. Niemczyk, F. Deppe, H. Huebl, E. P. Menzel, F. Hocke, M. J. Schwarz, J. J. Garcia-Ripoll, D. Zueco, T. Hümmer, E. Solano, A. Marx, R. Gross, Circuit quantum electrodynamics in the ultrastrong-coupling regime. *Nat. Phys.* **6**, 772–776 (2010).
13. A. Bayer, M. Pozimski, S. Schambeck, D. Schuh, R. Huber, D. Bougeard, C. Lange, Terahertz light-matter interaction beyond unity coupling strength. *Nano Lett.* **17**, 6340–6344 (2017).
14. B. Hacker, S. Welte, G. Rempe, S. Ritter, A photon-photon quantum gate based on a single atom in an optical resonator. *Nature* **536**, 193–196 (2016).
15. L. M. Duan, H. J. Kimble, Scalable photonic quantum computation through cavity-assisted interactions. *Phys. Rev. Lett.* **92**, 127902 (2004).
16. W.-Y. Liu, D.-N. Zheng, M. J. Hartmann, Quantum simulation with interacting photons. *J. Opt.* **18**, 104005 (2016).
17. A. Reiserer, G. Rempe, Cavity-based quantum networks with single atoms and optical photons. *Rev. Mod. Phys.* **87**, 1379–1418 (2015).
18. C. L. Degen, F. Reinhard, P. Cappellaro, Quantum sensing. *Rev. Mod. Phys.* **89**, 035002 (2017).

19. J. Ye, H. J. Kimble, H. Katori, Quantum state engineering and precision metrology using state-insensitive light traps. *Science* **320**, 1734–1738 (2008).
20. K. A. Gilmore, M. Affolter, R. J. Lewis-Swan, D. Barberena, E. Jordan, A. M. Rey, J. J. Bollinger, Quantum-enhanced sensing of displacements and electric fields with two-dimensional trapped-ion crystals. *Science* **373**, 673–678 (2021).
21. E. Pedrozo-Peñafiel, S. Colombo, C. Shu, A. F. Adiyatullin, Z. Li, E. Mendez, B. Braverman, A. Kawasaki, D. Akamatsu, Y. Xiao, V. Vuletić, Entanglement on an optical atomic-clock transition. *Nature* **588**, 414–418 (2020).
22. J. Majer, J. M. Chow, J. M. Gambetta, J. Koch, B. R. Johnson, J. A. Schreier, L. Frunzio, D. I. Schuster, A. A. Houck, A. Wallraff, A. Blais, M. H. Devoret, S. M. Girvin, R. J. Schoelkopf, Coupling superconducting qubits via a cavity bus. *Nature* **449**, 443–447 (2007).
23. R. Houdré, C. Weisbuch, R. P. Stanley, U. Oesterle, P. Pellandini, M. Illegems, Measurement of cavity-polariton dispersion curve from angle-resolved photoluminescence experiments. *Phys. Rev. Lett.* **73**, 2043–2046 (1994).
24. A. Polman, M. Kociak, F. J. García de Abajo, Electron-beam spectroscopy for nanophotonics. *Nat. Mater.* **18**, 1158–1171 (2019).
25. F. J. García de Abajo, V. Di Giulio, Optical excitations with electron beams: Challenges and opportunities. *ACS Photonics* **8**, 945–974 (2021).
26. O. L. Krivanek, N. Dellby, J. A. Hachtel, J. C. Idrobo, M. T. Hotz, B. Plotkin-Swing, N. J. Bacon, A. L. Bleloch, G. J. Corbin, M. V. Hoffman, C. E. Meyer, T. C. Lovejoy, Progress in ultrahigh energy resolution EELS. *Ultramicroscopy* **203**, 60–67 (2019).
27. A. B. Yankovich, B. Munkhbat, D. G. Baranov, J. Cuadra, E. Olsén, H. Lourenço-Martins, L. H. G. Tizei, M. Kociak, E. Olsson, T. Shegai, Visualizing spatial variations of plasmon-exciton polaritons at the nanoscale using electron microscopy. *Nano Lett.* **19**, 8171–8181 (2019).
28. O. Bitton, S. N. Gupta, L. Houben, M. Kvapil, V. Křápek, T. Šikola, G. Haran, Vacuum Rabi splitting of a dark plasmonic cavity mode revealed by fast electrons. *Nat. Commun.* **11**, 487 (2020).
29. K. Wang, R. Dahan, M. Shentcis, Y. Kauffmann, A. Ben Hayun, O. Reinhardt, S. Tsesses, I. Kaminer, Coherent interaction between free electrons and a photonic cavity. *Nature* **582**, 50–54 (2020).
30. O. Kfir, H. Lourenço-Martins, G. Storeck, M. Sivis, T. R. Harvey, T. J. Kippenberg, A. Feist, C. Ropers, Controlling free electrons with optical whispering-gallery modes. *Nature* **582**, 46–49 (2020).
31. Y. Kurman, R. Dahan, H. H. Sheinfux, K. Wang, M. Yannai, Y. Adiv, O. Reinhardt, L. H. G. Tizei, S. Y. Woo, J. Li, J. H. Edgar, M. Kociak, F. H. L. Koppens, I. Kaminer, Spatiotemporal imaging of 2D polariton wave packet dynamics using free electrons. *Science* **372**, 1181–1186 (2021).
32. S. Meuret, L. H. G. Tizei, F. Houdellier, S. Weber, Y. Auad, M. Tencé, H. C. Chang, M. Kociak, A. Arbouet, Time-resolved cathodoluminescence in an ultrafast transmission electron microscope. *Appl. Phys. Lett.* **119**, 062106 (2021).
33. M. Solà-García, K. W. Mauser, N. van Nielen, T. Coenen, S. Meuret, A. Polman, Pump-probe cathodoluminescence microscopy. arxiv:2112.03034 [physics.ins-det] (2 December 2021).
34. A. Feist, K. E. Echternkamp, J. Schauss, S. V. Yalunin, S. Schäfer, C. Ropers, Quantum coherent optical phase modulation in an ultrafast transmission electron microscope. *Nature* **521**, 200–203 (2015).
35. O. Kfir, Entanglements of electrons and cavity photons in the strong-coupling regime. *Phys. Rev. Lett.* **123**, 103602 (2019).
36. V. Di Giulio, M. Kociak, F. J. G. de Abajo, Probing quantum optical excitations with fast electrons. *Optica* **6**, 1524 (2019).
37. R. Dahan, A. Gorlach, U. Haeusler, A. Karnieli, O. Eyal, P. Yousefi, M. Segev, A. Arie, G. Eisenstein, P. Hommelhoff, I. Kaminer, Imprinting the quantum statistics of photons on free electrons. *Science* **373**, eabj7128 (2021).
38. A. Gorlach, A. Karnieli, R. Dahan, E. Cohen, A. Pe'er, I. Kaminer, Ultrafast non-destructive measurement of the quantum state of light using free electrons. arXiv:2012.12069 [quant-ph] (22 December 2020).
39. A. Gover, A. Yariv, Free-electron-bound-electron resonant interaction. *Phys. Rev. Lett.* **124**, 064801 (2020).
40. R. Ruimy, A. Gorlach, C. Mechel, N. Rivera, I. Kaminer, Toward atomic-resolution quantum measurements with coherently shaped free electrons. *Phys. Rev. Lett.* **126**, 233403 (2021).
41. Z. Zhao, X. Q. Sun, S. Fan, Quantum entanglement and modulation enhancement of free-electron-bound-electron interaction. *Phys. Rev. Lett.* **126**, 233402 (2021).
42. B. Zhang, D. Ran, R. Iancu, A. Friedman, J. Scheuer, A. Yariv, A. Gover, Quantum state interrogation using a preshaped free electron wavefunction. *Phys. Rev. Res.* **4**, 033071 (2022).
43. J. Lim, Y. S. Ang, L. K. Ang, L. J. Wong, Control of atom-photon interactions with shaped quantum electron wavepackets. arXiv:2111.13317 [quant-ph] (26 November 2021).
44. E. Arqué López, V. Di Giulio, F. J. García de Abajo, Atomic Floquet physics revealed by free electrons. *Phys. Rev. Res.* **4**, 013241 (2022).
45. B. W. Shore, P. L. Knight, The Jaynes-Cummings model. *J. Mod. Opt.* **40**, 1195–1238 (1993).
46. E. T. Jaynes, F. W. Cummings, Comparison of quantum and semiclassical radiation theories with application to the beam maser. *Proc. IEEE* **51**, 89–109 (1963).
47. B. Zhang, D. Ran, R. Iancu, A. Friedman, J. Scheuer, A. Yariv, A. Gover, Quantum wave-particle duality in free-electron-bound-electron interaction. *Phys. Rev. Lett.* **126**, 244801 (2021).
48. V. Di Giulio, F. J. G. de Abajo, Free-electron shaping using quantum light. *Optica* **7**, 1820–1830 (2020).
49. A. Ben Hayun, O. Reinhardt, J. Nemirovsky, A. Karnieli, N. Rivera, I. Kaminer, Shaping quantum photonic states using free electrons. *Sci. Adv.* **7**, 4270–4280 (2021).
50. I. I. Rabi, Space quantization in a gyration magnetic field. *Phys. Rev.* **51**, 652–654 (1937).
51. D. Braak, Integrability of the Rabi model. *Phys. Rev. Lett.* **107**, 100401 (2011).
52. A. Frisk Kockum, A. Miranowicz, S. De Liberato, S. Savasta, F. Nori, Ultrastrong coupling between light and matter. *Nat. Rev. Phys.* **1**, 19–40 (2019).
53. R. H. Dicke, Coherence in spontaneous radiation processes. *Phys. Rev.* **93**, 99–110 (1954).
54. J. J. Hopfield, Theory of the contribution of excitons to the complex dielectric constant of crystals. *Phys. Rev.* **112**, 1555–1567 (1958).
55. D. Press, S. Götzinger, S. Reitzenstein, C. Hofmann, A. Löffler, M. Kamp, A. Forchel, Y. Yamamoto, Photon antibunching from a single quantum-dot-microcavity system in the strong coupling regime. *Phys. Rev. Lett.* **98**, 117402 (2007).
56. E. Peter, P. Senellart, D. Martrou, A. Lemaître, J. Hours, J. M. Gérard, J. Bloch, Exciton-photon strong-coupling regime for a single quantum dot embedded in a microcavity. *Phys. Rev. Lett.* **95**, 067401 (2005).
57. T. Yoshie, A. Scherer, J. Hendrickson, G. Khitrova, H. M. Gibbs, G. Rupper, C. Ell, O. B. Shchekin, D. G. Deppe, Vacuum Rabi splitting with a single quantum dot in a photonic crystal nanocavity. *Nature* **432**, 200–203 (2004).
58. D. Englund, A. Faraon, I. Fushman, N. Stoltz, P. Petroff, J. Vučković, Controlling cavity reflectivity with a single quantum dot. *Nature* **450**, 857–861 (2007).
59. K. Hennessy, A. Badolato, M. Winger, D. Gerace, M. Atatüre, S. Gulde, S. Fält, E. L. Hu, A. Imamoglu, Quantum nature of a strongly coupled single quantum dot-cavity system. *Nature* **445**, 896–899 (2007).
60. P. Törmö, W. L. Barnes, Strong coupling between surface plasmon polaritons and emitters: A review. *Rep. Prog. Phys.* **78**, 013901 (2014).
61. O. Bitton, S. N. Gupta, G. Haran, Quantum dot plasmonics: From weak to strong coupling. *Nanophotonics* **8**, 559–575 (2019).
62. K. Santhosh, O. Bitton, L. Chuntonov, G. Haran, Vacuum Rabi splitting in a plasmonic cavity at the single quantum emitter limit. *Nat. Commun.* **7**, ncomms11823 (2016).
63. H. Groß, J. M. Hamm, T. Tufarelli, O. Hess, B. Hecht, Near-field strong coupling of single quantum dots. *Sci. Adv.* **4**, aar4906 (2018).
64. H. Leng, B. Szychowski, M. C. Daniel, M. Pelton, Strong coupling and induced transparency at room temperature with single quantum dots and gap plasmons. *Nat. Commun.* **9**, 4012 (2018).
65. J. J. Baumberg, J. Aizpurua, M. H. Mikkelsen, D. R. Smith, Extreme nanophotonics from ultrathin metallic gaps. *Nat. Mater.* **18**, 668–678 (2019).
66. Y. Yang, A. Massuda, C. Roques-Carmes, S. E. Kooi, T. Christensen, S. G. Johnson, J. D. Joannopoulos, O. D. Miller, I. Kaminer, M. Soljačić, Maximal spontaneous photon emission and energy loss from free electrons. *Nat. Phys.* **14**, 894–899 (2018).
67. A. Gubbens, M. Barfels, C. Trevor, R. Twisten, P. Mooney, P. Thomas, N. Menon, B. Kraus, C. Mao, B. McGinn, The GIF Quantum, a next generation post-column imaging energy filter. *Ultramicroscopy* **110**, 962–970 (2010).
68. M. Haruta, Y. Fujiyoshi, T. Nemoto, A. Ishizuka, K. Ishizuka, H. Kurata, Extremely low count detection for EELS spectrum imaging by reducing CCD read-out noise. *Ultramicroscopy* **207**, 112827 (2019).
69. V. Giovannetti, S. Lloyd, L. MacCone, Advances in quantum metrology. *Nat. Photonics* **5**, 222–229 (2011).
70. J. Verbeeck, D. Van Dyck, G. Van Tendeloo, Energy-filtered transmission electron microscopy: An overview. *Spectrochim. Acta Part B At. Spectrosc.* **59**, 1529–1534 (2004).
71. F. F. Krause, A. Rosenauer, J. Barthel, J. Mayer, K. Urban, R. E. Dunin-Borkowski, H. G. Brown, B. D. Forbes, L. J. Allen, Atomic resolution elemental mapping using energy-filtered imaging scanning transmission electron microscopy with chromatic aberration correction. *Ultramicroscopy* **181**, 173–177 (2017).
72. L. Gu, W. Sigle, C. T. Koch, J. Nelayah, V. Srot, P. A. van Aken, Mapping of valence energy losses via energy-filtered annular dark-field scanning transmission electron microscopy. *Ultramicroscopy* **109**, 1164–1170 (2009).
73. B. Schaffer, U. Hohenester, A. Trügler, F. Hofer, High-resolution surface plasmon imaging of gold nanoparticles by energy-filtered transmission electron microscopy. *Phys. Rev. B Condens. Matter Mater. Phys.* **79**, 041401 (2009).
74. S. Lichtert, J. Verbeeck, Statistical consequences of applying a PCA noise filter on EELS spectrum images. *Ultramicroscopy* **125**, 35–42 (2013).

75. M. V. Tsarev, A. Ryabov, P. Baum, Free-electron qubits and maximum-contrast attosecond pulses via temporal Talbot revivals. *Phys. Rev. Res.* **3**, 043033 (2021).
76. O. Reinhardt, C. Mechel, M. Lynch, I. Kaminer, Free-electron qubits. *Ann. Phys.* **533**, 2000254 (2021).
77. G. M. Vanacore, I. Madan, G. Berruto, K. Wang, E. Pomarico, R. J. Lamb, D. McGrouther, I. Kaminer, B. Barwick, F. J. García de Abajo, F. Carbone, Attosecond coherent control of free-electron wave functions using semi-infinite light fields. *Nat. Commun.* **9**, 2694 (2018).
78. K. E. Priebe, C. Rathje, S. V. Yalunin, T. Hohage, A. Feist, S. Schäfer, C. Ropers, Attosecond electron pulse trains and quantum state reconstruction in ultrafast transmission electron microscopy. *Nat. Photonics* **11**, 793–797 (2017).
79. Y. Morimoto, P. Baum, Diffraction and microscopy with attosecond electron pulse trains. *Nat. Phys.* **14**, 252–256 (2018).
80. R. Shiloh, T. Chlouba, P. Hommelhoff, Quantum-coherent light-electron interaction in a Scanning Electron Microscope. *Phys. Rev. Lett.* **128**, 235301 (2021).
81. E. Pomarico, I. Madan, G. Berruto, G. M. Vanacore, K. Wang, I. Kaminer, F. J. García De Abajo, F. Carbone, meV resolution in laser-assisted energy-filtered transmission electron microscopy. *ACS Photonics* **5**, 759–764 (2018).
82. B. Barwick, D. J. Flannigan, A. H. Zewail, Photon-induced near-field electron microscopy. *Nature* **462**, 902–906 (2009).
83. S. T. Park, M. Lin, A. H. Zewail, Photon-induced near-field electron microscopy (PINEM): Theoretical and experimental. *New J. Phys.* **12**, 123028 (2010).
84. Y. Adiv, H. Hu, S. Tsesses, R. Dahan, K. Wang, Y. Kurman, H. Chen, X. Lin, G. Bartal, I. Kaminer, Observation of 2D Cherenkov radiation and its Quantized Photonic Nature Using Free-Electrons, in *Conference on Lasers and Electro-Optics* (Optica Publishing Group, 2021).
85. R. Dahan, S. Nehemia, M. Shentcic, O. Reinhardt, Y. Adiv, X. Shi, O. Be'er, M. H. Lynch, Y. Kurman, K. Wang, I. Kaminer, Resonant phase-matching between a light wave and a free-electron wavefunction. *Nat. Phys.* **16**, 1123–1131 (2020).
86. A. Karnieli, S. Tsesses, R. Yu, N. Rivera, Z. Zhao, A. Arie, S. Fan, I. Kaminer, Probing strongly coupled light-matter interactions using quantum free electrons, in *2022 Conference on Lasers and Electro-Optics* (Optica Publishing Group, 2022); https://opg.optica.org/abstract.cfm?uri=CLEO_QELS-2022-FTh5L.4.
87. G. Baranes, R. Ruimy, A. Gorlach, I. Kaminer, Free electrons can induce entanglement between photons. *npj Quantum Inf.* **8**, 32 (2022).
88. A. Feist, G. Huang, G. Arend, Y. Yang, J.-W. Henke, A. Sajid Raja, F. J. Kappert, R. N. Wang, H. Lourenço-Martins, Z. Qiu, J. Liu, O. Kfir, T. J. Kippenberg, C. Ropers, Cavity-mediated electron-photon pairs. *Science*, **377**, 777 (2022).
89. A. Karnieli, N. Rivera, A. Arie, I. Kaminer, Superradiance and subradiance due to quantum interference of entangled free electrons. *Phys. Rev. Lett.* **127**, 060403 (2021).
90. M. Scala, B. Militello, A. Messina, J. Piilo, S. Maniscalco, Microscopic derivation of the Jaynes-Cummings model with cavity losses. *Phys. Rev. A At. Mol. Opt. Phys.* **75**, 013811 (2007).

Acknowledgments

Funding: This work was funded by the Gordon and Betty Moore Foundation grant number GBMF4744, by the European Research Council grant number NanoEP 851780, and by the Israel Science Foundation grant number 1415/17. A.K. and S.T. acknowledge support from the Adams Fellowship of the Israeli Academy of Sciences and Humanities. **Author contributions:** A.K. devised the theoretical formalism. A.K., S.T., and R.Y. equally contributed to the proposal of applications for quantum sensing. N.R. and Z.Z. participated in discussions. A.A., S.F., and I.K. supervised the project. **Competing interests:** The authors declare that they have no competing interests. **Data and Materials availability:** All data needed to evaluate the conclusions in the paper are present in the paper and/or the Supplementary Materials.

Submitted 30 May 2022

Accepted 28 November 2022

Published 4 January 2023

10.1126/sciadv.add2349